

ARTICLE

<https://doi.org/10.1038/s41467-019-14053-w>

OPEN

Coherent spin control of s-, p-, d- and f-electrons in a silicon quantum dot

R.C.C. Leon^{1*}, C.H. Yang¹, J.C.C. Hwang^{1,6}, J. Camirand Lemyre², T. Tanttu¹, W. Huang¹, K.W. Chan¹, K.Y. Tan³, F.E. Hudson¹, K.M. Itoh⁴, A. Morello¹, A. Laucht¹, M. Pioro-Ladrière^{2,5}, A. Saraiva^{1*} & A.S. Dzurak¹

Once the periodic properties of elements were unveiled, chemical behaviour could be understood in terms of the valence of atoms. Ideally, this rationale would extend to quantum dots, and quantum computation could be performed by merely controlling the outer-shell electrons of dot-based qubits. Imperfections in semiconductor materials disrupt this analogy, so real devices seldom display a systematic many-electron arrangement. We demonstrate here an electrostatically confined quantum dot that reveals a well defined shell structure. We observe four shells (31 electrons) with multiplicities given by spin and valley degrees of freedom. Various fillings containing a single valence electron—namely 1, 5, 13 and 25 electrons—are found to be potential qubits. An integrated micromagnet allows us to perform electrically-driven spin resonance (EDSR), leading to faster Rabi rotations and higher fidelity single qubit gates at higher shell states. We investigate the impact of orbital excitations on single qubits as a function of the dot deformation and exploit it for faster qubit control.

¹Centre for Quantum Computation and Communication Technology, School of Electrical Engineering and Telecommunications, The University of New South Wales, Sydney, NSW 2052, Australia. ²Institut Quantique et Département de Physique, Université de Sherbrooke, Sherbrooke, Québec J1K 2R1, Canada. ³QCD Labs COMP Centre of Excellence, Department of Applied Physics, Aalto University, 00076 Aalto, Finland. ⁴School of Fundamental Science and Technology, Keio University, 3-14-1 Hiyoshi, Kohoku, Yokohama 223-8522, Japan. ⁵Quantum Information Science Program, Canadian Institute for Advanced Research, Toronto, ON M5G 1Z8, Canada. ⁶Present address: Research and Prototype Foundry, The University of Sydney, Sydney, NSW 2006, Australia. *email: r.leon@unsw.edu.au; a.saraiva@unsw.edu.au; a.dzurak@unsw.edu.au

Qubit architectures based on electron spins in gate-defined silicon quantum dots benefit from a high level of controllability, where single and multi-qubit coherent operations are realised solely with electrical and magnetic manipulation. Furthermore, their direct compatibility with silicon microelectronics fabrication offers unique scale-up opportunities¹. However, fabrication reproducibility and disorder pose challenges for single-electron quantum dots. Even when the single-electron regime is achievable, the last electron often is confined in a very small region, limiting the effectiveness of electrical control and interdot tunnel coupling. Many-electron quantum dots were proposed as a qubit platform decades ago², with the potential of resilience to charge noise^{3,4} and a higher tunable tunnel coupling strength to other qubits⁵. In the multielectron regime, the operation of a quantum dot qubit is more sensitive to its shape. If it is axially symmetric, the orbital energy levels will be quasi-degenerate^{6–8}, which is detrimental for quantum computing. On the contrary, if the quantum dot is very elongated, a regular shell structure will not form, and it becomes difficult to identify a priori what charge configurations will lead to spin-1/2 systems suitable for quantum computing^{2,9,10}.

Results

Filling s-, p-, d- and f-orbitals in a silicon quantum dot. The scanning electron microscope (SEM) image in Fig. 1a shows a silicon metal-oxide-semiconductor (Si-MOS) device that forms a quantum dot at the Si/SiO₂ interface under gate G1, separated from the reservoir by a barrier that is controlled by gate G2—see Fig. 1b for a cross-sectional representation. We first study the electronic structure of the dot from its charge stability diagram, using the technique from ref. ¹¹, which maps out each electron transition between quantum dot and reservoir as a function of gate potentials. Figure 1c shows a well ordered set of electron transitions, revealing a quantum dot that can be occupied by up to 31 electrons with no significant evidence of disorder in the form of reconfiguration of charge traps in the oxide or at the Si/SiO₂ interface (which would lead to the occurrence of addition energies that do not follow a periodic rule). This occupancy range is slightly better than other devices based on similar technology¹². Additional charge transitions in Fig. 1c (faint nearly-horizontal lines) arise from states between the reservoir and the quantum dot and do not affect the qubit operation. Lowering the voltage of gate G2 confines the quantum dot further and changes its eccentricity in the x-y plane.

Following the red dashed line in Fig. 1c allows us to investigate the addition energies, i.e., the energy necessary to add the N -th electron to a dot that contains $N-1$ electrons, as plotted in Fig. 1d. The first noticeable effect is that the charging energy is roughly inversely proportional to the number of electrons, which is a consequence of the dot size becoming larger as the dot fills up. Furthermore, very distinct peaks appear at transitions $4 \rightarrow 5$, $12 \rightarrow 13$ and $24 \rightarrow 25$. To understand the significance of these electron numbers, one may refer to the Fock-Darwin energy levels^{13,14}, where the internal spin (\uparrow, \downarrow) and valley (v_+, v_-) quantum numbers give the multiplicity of each orbital state in a two-dimensional quantum dot. As a result, a full shell is formed when there are 4, 12 and 24 electrons in the 2D quantum dot, and so an extra energy, corresponding to the orbital level splitting, must be supplied in order to begin filling the next shell. The filling of three complete electron shells has previously been observed in a GaAs quantum dot⁶, where the single-valley nature of the semiconductor leads to a filled third shell at $N=12$ electrons, but until now has not been observed in a silicon device. The observed shell filling is analogous to the aufbau principle of atomic physics, that allows us to construct the electronic structure

of many-electron atoms in terms of occupation of the atomic electron levels from bottom up.

As well as the large jumps in addition energy observed after complete shells are filled, a finer structure at intermediate fillings is also present due to the valley splitting Δ_{VS} ¹⁵, the energy difference between excitations along the major and minor axes of the elliptical quantum dot¹⁶, Δ_{xy} , and electronic quantum correlations¹⁷, dominated by the exchange coupling J . These energy scales are much smaller than the shell excitation, so that we can identify each set of levels by a principal quantum number. Each shell is spanned by the valley^{18–20}, spin and azimuthal²¹ quantum numbers. For this particular quantum dot, Δ_{VS} and Δ_{xy} may be estimated^{12,19} and both are of the order of hundreds of μ eV, which is consistent with typical observations for quantum dots with similar designs²⁰. Since both splittings are similar in magnitude, it is difficult to label the inner shell structure based solely on the addition energy diagram.

Magnetospectroscopy of the electron transitions (Fig. 1e) indicates the variation in total spin S between consecutive fillings by tracking the addition energy as a function of external magnetic field strength B_0 (see ref. ²² for a detailed method of extracting total spin S from magnetospectroscopy). A negative slope indicates an increase in total S , and a positive slope represents a decrease in total spin. At lower electron occupancies, S alternates between $\frac{1}{2}$ and 0, with cumulative spin state S presented in Fig. 1f. This indicates that the sequential electron loading favours anti-parallel spin states, implying $J \ll \Delta_{xy}, \Delta_{VS}$. As the electron number increases, Hund's rule applies as some of the electrons are loaded as parallel spins ($S=1$ or $\frac{3}{2}$ states), indicating $J > \Delta_{xy}, \Delta_{VS}$ in these cases. Notice that in a few instances, a kink is observed, which indicates that the Zeeman splitting has become larger than some orbital or valley splitting, so that the electron occupies the higher orbital and creates a state with higher S .

The observation of $S=1$ spin states is potentially significant, in the context of the study of symmetry-protected topological phases of $S=1$ spin chains with antiferromagnetic Heisenberg coupling. As conjectured by Haldane²³, such $S=1$ spin chains possess a fourfold degenerate ground state, protected by a topological gap to higher excited states. Finite-length chains exhibit fractionalized $S=1/2$ states at their ends, which could be exploited for robust quantum computing schemes^{24–26}. The experimental realization of controllable $S=1$ Haldane chains, however, has remained a formidable challenge²⁷. In semiconductor quantum dots, methods to locally control and read-out chains of spins are now mature. Engineering $S=1$ with the natural Heisenberg exchange interaction in this system might open exciting opportunities for future studies in this field.

Operation of single-valence multielectron spin qubits. We now examine the spins of monovalent dot occupations as potential qubits, i.e., the first electron of each shell $N=1, 5, 13$ and 25 , which we call s-, p-, d- and f-electrons, respectively, in reference to the electronic orbitals²⁸. To demonstrate single-qubit control, we designed this device with the capability to perform electrically-driven spin resonance (EDSR). A cobalt micromagnet positioned near the quantum dot induces a magnetic field gradient. An external uniform magnetic field $B_0 = 1.4$ T provides a Zeeman splitting between spin states for spin to charge conversion read-out²⁹. This field also fully magnetises the micromagnet (cobalt is fully magnetised at $B_0 \sim 0.4 - 0.5$ T), leading to a field gradient of ~ 1 T/ μ m in the direction transverse to the quantization axis. This provides the means to drive spin flips without the need for an AC magnetic field^{30–32}. Instead, a ~ 40 GHz sinusoidal voltage is applied directly to the magnet. The antenna-like structure creates an AC electric field at the quantum dot, so that the electron

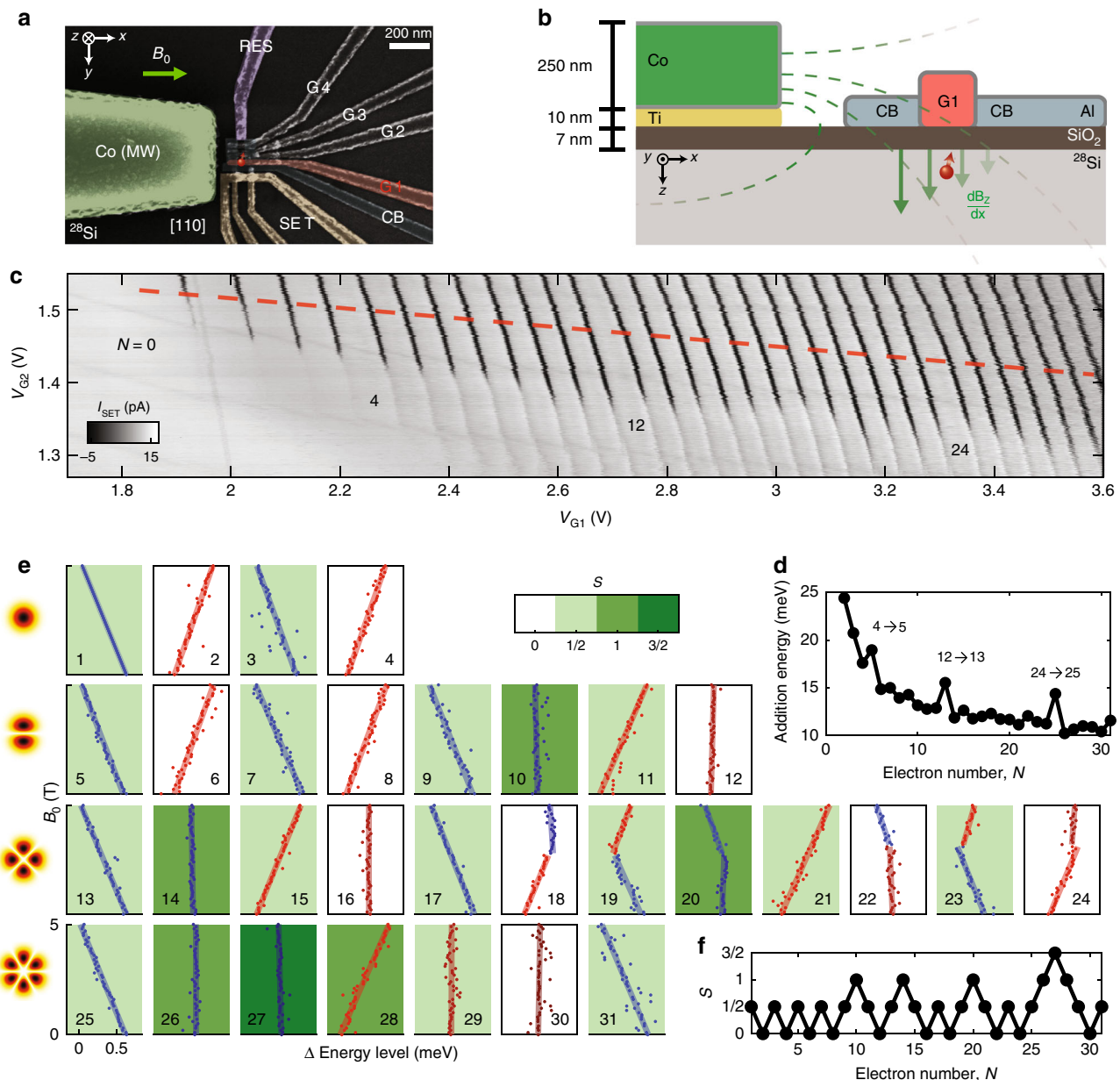


Fig. 1 Device overview and electron occupancy measurement. **a** False-coloured SEM image of a nominally identical device to that reported here. A quantum dot is formed under gate G1 (red), in the location marked by the red symbol. Gate RES is connected to an n-doped reservoir to load/unload electrons to/from the quantum dot, with tunnel rates controlled by G2, G3 and G4. Gate CB serves as a confinement barrier. The cobalt (Co) structure at the left of the image acts as both a micromagnet and electrode for EDSR control (green). **b** Cross-sectional schematic of the device, fabricated on a purified Silicon-28 epi-layer (800 ppm). **c** Charge stability map of the quantum dot at $B_0 = 0$ T, produced by plotting the pulsed lock-in signal from SET sensor I_{pulsed} vs V_{G1} and V_{G2} . A square wave with peak-to-peak amplitude of 2 mV is applied to G1 for lock-in excitation. Dynamic compensation is applied to the SET sensor to maintain a high read-out sensitivity. Electron numbers N for full shells are marked on the diagram. **d** Charging energies along the red line in (c) in the tightly confined regime. **e** Magnetotransport plots of the first 31 electrons occupied in the quantum dot, up to $B_0 = 5$ T, with background colour of each plot representing spin state S at $B_0 = 0$ T. Change in addition energies with magnetic field are measured and fitted with straight lines. Since the charging energy is measured only from the second electron, the first electron is depicted by a straight line with no data. Each row of the array of plots belongs to the same shell, while each column has the same number of valence electrons in its outer shell. The cartoon on the left gives an example of the electron wavefunction for each shell. **f** Spin state of each electron occupancy extracted from (e).

wavefunction oscillates spatially within the slanted magnetic field, which drives Rabi oscillations of the qubit^{33–35}.

In order to initialize, control and read-out the spins, the pulse sequence depicted in Fig. 2a is performed. The amplitude and duration of the driving AC electric field is used to implement various single-qubit logical gates. The fidelity of these qubit operations under the decoherence introduced by the environment

is probed by a randomized benchmarking protocol^{36,37}, shown in the Supplementary Fig. 3 for s-, p-, and d-electrons. Single-qubit elementary gate fidelities improve from 98.5% to 99.7% and 99.5% when the electron occupancy increases from 1 to 5 and 13 electrons. Part of the reason for this improvement is the reduction of the quantum dot confinement at higher occupations—the Coulomb repulsion due to electrons in inner shells leads to a

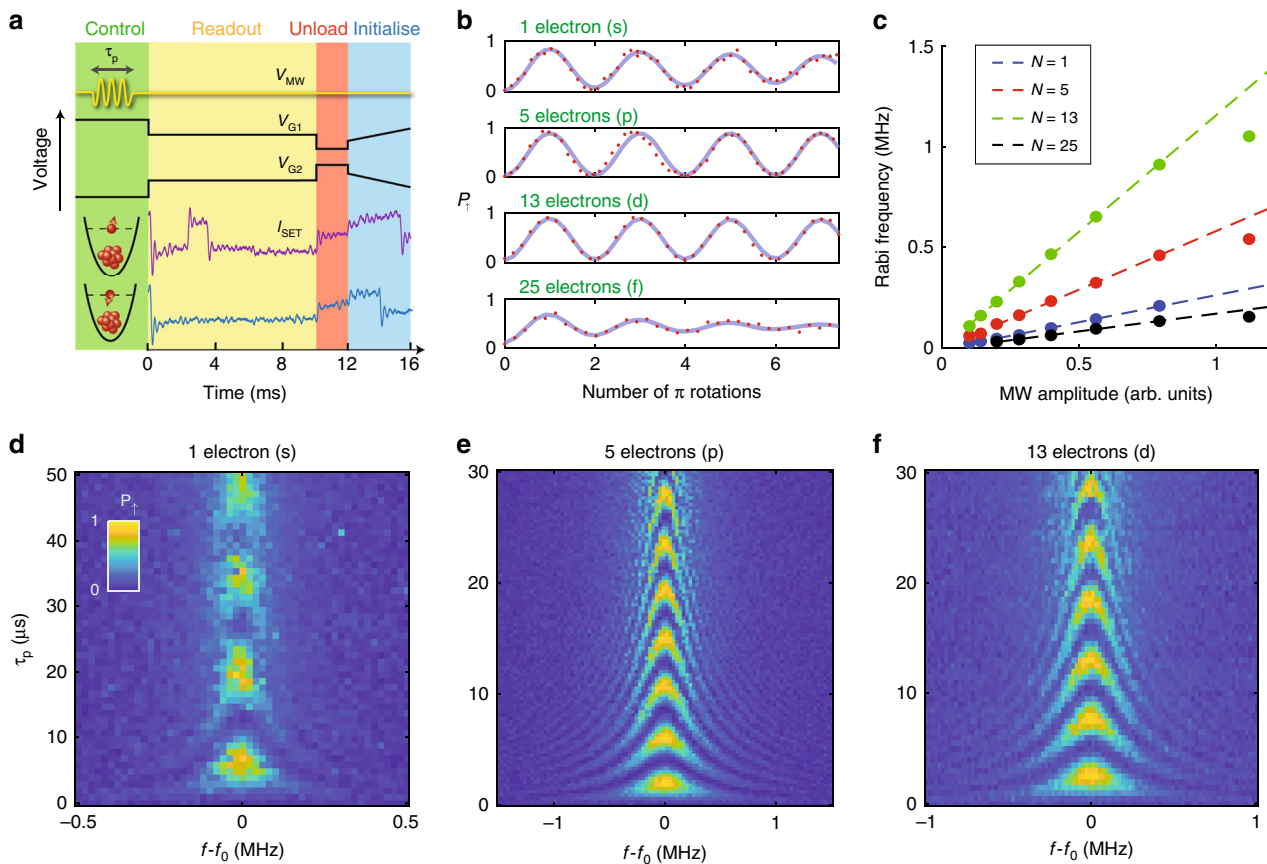


Fig. 2 Coherent spin control. **a** Gate and microwave pulse sequence for single-qubit control and read-out. The lower section shows the change in SET current when a valence electron is in either a spin up or down state. **b** Rabi oscillation of the probability of measuring a spin up P_{\uparrow} for $N = 1, 5, 13$ and 25 electrons, under the same driving power from the microwave source. Traces for s, p, d electrons are extracted from **(d-f)** at $f = f_0$, fitted using $P_{\uparrow} = A \cos(2\pi f_{\text{Rabi}} t) e^{-t/T_2^{\text{Rabi}}} + c$, where A and c are related to the measurement visibility. Horizontal axis is number of π rotations ($\frac{t_p}{\pi}$) of each oscillation. **c** Rabi frequencies as a function of applied microwave power, at different electron numbers N . **d-f** Probability of spin up as a function of ESR frequency detuning and duration of microwave pulse for **(d)** $N = 1$, **(e)** $N = 5$ and **(f)** $N = 13$ electrons, performed along the grey dashed line in Fig. 3e, f, h, i, k, l, which correspond to the highest Q-factor operating points for each electron occupancy. Resonance frequencies f_0 for $N = 1, 5$ and 13 are $41.829, 41.879$ and 41.827 GHz, respectively.

shallower confinement, thus reducing charging and orbital energies (Fig. 1d) and ultimately leading to faster Rabi frequencies f_{Rabi} . We note that this effect cannot be compensated by an increase in the driving power (amplitude of the oscillating electric field) because the Rabi frequency saturates at high power (Fig. 2c).

At s-, p-, d-, and f-electron occupations, Rabi frequencies increase linearly with microwave amplitude (Fig. 2c). As more electrons occupy the quantum dot, their wavefunction size increases and confinement energy decreases, hence leading to a higher effective oscillating magnetic field via EDSR³³. At the f-electron, other effects such as multiple relaxation hot spots prevent an optimal voltage configuration for the qubit, resulting in an inefficient Rabi drive.

One should note that the Dresselhaus spin-orbit coupling has very distinct impact on each valley state, which could potentially affect EDSR if it was driven by the material spin-orbit coupling^{38,39}. Since our EDSR approach adopts an inhomogeneous magnetic field induced by a micromagnet, however, we expect that possible suppressions of spin-orbit effects by valley interference are overcome by the field gradient. In other words, the observed improvement of the Rabi oscillations is unlikely to largely stem from variations in the valley structure among shells.

A more intuitive way to probe the effects of faster gating times is by measuring the Q-factor ($Q = T_2^{\text{Rabi}}/T_{\pi}$) of Rabi oscillations

of 1, 5, 13 and 25 electrons (see Fig. 2b). The amplitude for s and f electrons is damped quickly enough that after 7π rotations a noticeable decrease in coherence is observed. We extract $Q = 14$ for s electrons and $Q = 3.4$ for f electrons. Conversely, p and d electrons show barely visible decay. The minimum observed Q-factor for either p or d electrons, obtained in a different voltage configuration, was $Q > 34$ (this value is strongly impacted by gate bias voltages and power of the EDSR driving field). This effect also cannot be compensated with the driving power because the Q-factor is not significantly improved at any particular value of the microwave amplitude (see Supplementary Note 2).

Moreover, Rabi chevron plots in Fig. 2d-f show a visible improvement in the quality of both $N = 5$ and 13 electrons compared with $N = 1$. Further coherence time measurements were also performed, with T_2^* ranging from 5.7 to 18.1 μ s and T_2^{Hahn} between 21.6 and 68.5 μ s (see Supplementary Note 4 for details)^{40,41}. We highlight that the coherence times of p and d electrons still outperform the single spin coherence obtained in natural silicon⁴², indicating that closed shell electrons are not a leading source of dephasing noise. The direct quantitative comparison between coherence times is not a precise measure of robustness against noise because the total acquisition time may impact the estimate of T_2^* , but we conclude that no impact on T_2^* is observed due to the electrons which comprise a closed shell.

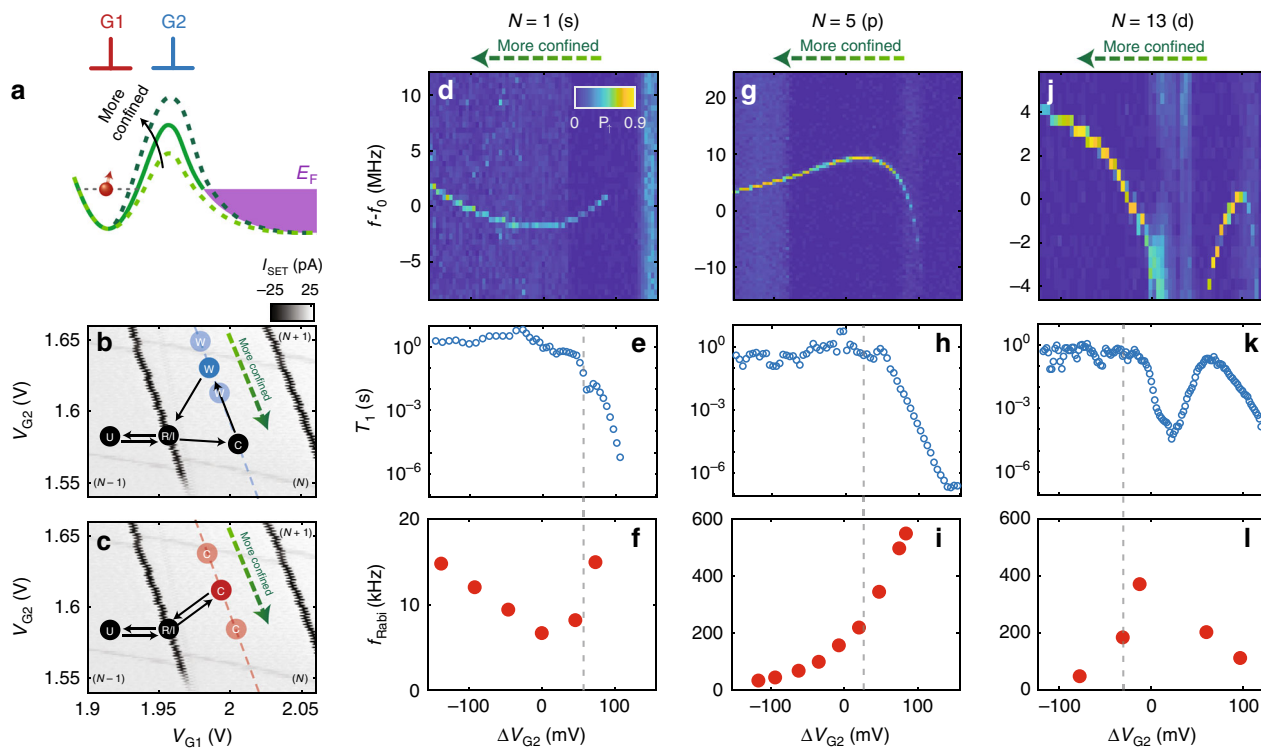


Fig. 3 Stark shift, tunable Rabi frequency and relaxation time. **a** Schematic representation of the quantum device energy band diagram. G2 voltage varies in order to change the quantum dot size and tunnel rate to the reservoir (purple). Compensating voltage is also applied to G1 to maintain the quantum dot energy level relative to the Fermi level E_F . **b, c** Schematics of the pulse sequences for **(b)** T_1 relaxation, and **(c)** Rabi control experiment. The qubit control point varies along the dashed line inside the charge stability diagram, parallel to the charge transitions, with electron occupancy either $N=1, 5$ or 13 . **d** Non-linear Stark shift of qubit resonance frequency is observed when the qubit control point changes along dashed line in **(b)** and **(c)**, for $N=1$ electron. At certain voltage levels, the resonance frequency shifts dramatically and eventually qubit read-out is unachievable. **e** Correlation is observed between the magnitude of the differential ESR resonance frequency ($f - f_0$) and qubit relaxation time T_1 . **f** Correlation is also observed between $f - f_0$ and Rabi frequency f_{Rabi} . There is a qualitative correlation between the maximum Rabi frequency and the non-linearity of the Stark shift. **g-l** Stark shift, T_1 and Rabi frequencies as plotted in Figs. **(d-f)**, but for **(g-i)** $N=5$ and **(j-l)** 13 electrons. Examples of advantageous qubit operation voltages, where a balance exists between fast Rabi oscillation and long spin lifetime, are drawn as grey vertical lines in the figure. $f_0 = 41.835, 41.870, 41.826$ GHz for $N=1, 5$ and 13 electrons, respectively.

The small variations in coherence are largely compensated by the enhanced Rabi frequency for p and d electrons, which explains the improved qubit performances.

Although Rabi oscillations are visible for $N=25$ in Fig. 2b, we observed its optimal π -pulse time and T_2^{Rabi} to be similar to $N=1$. This indicates that higher shell numbers do not necessary benefit qubit operation, as more relaxation hot spots will arise with the increased multiplicity of the shell states¹².

Impact of excited states on multielectron qubits. Although multielectron quantum dots can be exploited to improve qubit performance, they raise new questions regarding the many-body physics of these dots. One particular concern is that the presence of low-lying excited orbital states may interfere with the spin dynamics. We track the excited states by altering the dot aspect ratio without changing its occupancy⁴³ (see schematic in Fig. 3a), by adjusting the G1 and G2 gate voltages as indicated in Fig. 3b and c. We first measure the qubit resonance frequencies while varying the dot shape (Fig. 3c). This frequency is impacted by variations in g-factor and micromagnet field as the dot is distorted by the external electric field—we collectively refer to these effects as Stark shift. Linear Stark shift should be observed since the control point of the quantum dot is far detuned from any charge transition. Instead, non-linear Stark shifts are observed for $N=1$ (Fig. 3d), $N=5$ (Fig. 3g) and $N=13$ electrons (Fig. 3j). Although such phenomenon can be partially explained by change

in magnetic field experienced by the quantum dot along the x -direction, a significant drop in resonance frequencies is observed for $N=5$ (Fig. 3g) and 13 electrons (Fig. 3j) at $\Delta V_{G2} > 100$ mV and $20 \text{ mV} < \Delta V_{G2} < 60$ mV, respectively.

To investigate this further, we measure the spin relaxation time T_1 using the pulse sequence in Fig. 3b, as shown in Fig. 3e, h, k. A clear correlation between the drop in T_1 and regions with a highly non-linear Stark shift is similar to previous literature^{12,44,45}. This indicates the presence of an excited orbital or valley state nearby the Zeeman excitation, resulting in a reduction of T_1 .

Since the virtual excited state (either valley⁴⁶ or orbital^{47,48}) plays an essential role in EDSR, the excitation energy directly influences the qubit Rabi frequencies. Performing the pulse sequence in Fig. 3c, we observe an enhancement of one order of magnitude for the Rabi frequencies of p and d orbitals (Figs. 3f, i, l) correlated to the drop in T_1 . We also notice that the Larmor frequency and the Rabi frequency as a function of ΔV_{G2} in this experiment may be non-monotonic in some charge configurations, with a discernible correlation between their extrema. These are indications that the p and d spins are coupled to excited states of a different nature to those for s electrons. There are no charge transitions (or visible features in the charge stability diagram), indicating that the ground state configuration is left unchanged. Note that some Rabi frequency enhancement is also observed for the $N=1$ electron configuration, but it is an order of magnitude lower than for $N=5$ and 13 electrons.

We may exploit this control over the excitation spectrum to induce fast relaxation on demand for qubit initialization, to operate the qubit where f_{Rabi} is high, and to store it in a configuration where T_1 is long. The power of the EDSR drive only impacts the observed Q -factor value up to a factor of 2 (see Supplementary Fig. 2), in contrast to recent observations in depletion mode quantum dot experiments⁴⁹ where an order of magnitude difference in Q -factors were observed.

The additional relaxation hotspot around $\Delta V_{\text{G}1} = 10$ mV for the d-shell qubit in Fig. 3k is most likely due to the increased number of near-degenerate orbitals present, which implies more pathways for qubit relaxation. This near-degeneracy could also be related to why the 14 electron configuration follows Hund's rule to give a $S = 1$ ground state^{9,50} (see Fig. 1f). We note that these higher total spin states are observed to also be coherently drivable, but a detailed study of these high-spin states exceeds the scope of our present work (see Supplementary Fig. 5c & d).

Discussion

The results presented here experimentally demonstrate that robust spin qubits can be implemented in multielectron quantum dots up to at least the third valence shell. Their utility indicates that it is not necessary to operate quantum dot qubits at single-electron occupancy, where disorder can degrade their reliability and performance. Furthermore, the larger size of multielectron wavefunctions combined with EDSR can enable higher control fidelities, and should also enhance exchange coupling between qubits⁵¹. A multielectron system results in a richer many-body excitation spectrum, which can lead to higher Rabi frequencies for fast qubit gates and enhanced relaxation rates for rapid qubit initialization. Future experiments exploring two-qubit gates using multielectron quantum dots will extend this understanding of electronic valence to interpret bonding between neighbouring dots in terms of their distinct orbital states. The controllability of the excitation spectrum should also allow for different regimes of electron pairing, including a possible singlet-triplet inversion⁵⁰, mimicking the physics of paramagnetic bonding⁵².

Data availability

The data that support the findings of this study are available from the authors on reasonable request, see author contributions for specific data sets.

Received: 10 June 2019; Accepted: 11 December 2019;

Published online: 11 February 2020

References

1. Vandersypen, L. M. K. et al. Interfacing spin qubits in quantum dots and donors - hot, dense, and coherent. *npj Quantum Inf.* **3**, 34 (2017).
2. Hu, X. & Das Sarma, S. Spin-based quantum computation in multielectron quantum dots. *Phys. Rev. A* **64**, 042312 (2001).
3. Barnes, E., Kestner, J. P., Nguyen, N. T. T. & Sarma, S. D. Screening of charged impurities with multielectron singlet-triplet spin qubits in quantum dots. *Phys. Rev. B* **84**, 235309 (2011).
4. Bakker, M. A., Mehl, S., Hiltunen, T., Harju, A. & Di-Vincenzo, D. P. Validity of the single-particle description and charge noise resilience for multielectron quantum dots. *Phys. Rev. B* **91**, 155425 (2015).
5. Harvey-Collard, P. et al. Coherent coupling between a quantum dot and a donor in silicon. *Nat. Commun.* **8**, 1029 (2017).
6. Tarucha, S., Austing, D. G., Honda, T., Van Der Hage, R. J. & Kouwenhoven, L. P. Shell filling and spin effects in a few electron quantum dot. *Phys. Rev. Lett.* **77**, 3613–3616 (1996).
7. Kouwenhoven, L. P. et al. Excitation spectra of circular, few-electron quantum dots. *Science* **278**, 1788–1792 (1997).
8. Rontani, M. et al. Full configuration interaction approach to the few-electron problem in artificial atoms. *J. Chem. Phys.* **124**, 124102 (2006).
9. Deng, K., Calderon-Vargas, F., Mayhall, N. J. & Barnes, E. Negative exchange interactions in coupled few-electron quantum dots. *Phys. Rev. B* **97**, 245301 (2018).
10. Malinowski, F. K. et al. Spin of a multielectron quantum dot and its interaction with a neighboring electron. *Phys. Rev. X* **8**, 11045 (2018).
11. Yang, C. H., Lim, W. H., Zwanenburg, F. A. & Dzurak, A. S. Dynamically controlled charge sensing of a few-electron silicon quantum dot. *AIP Adv.* **1**, 42111 (2011).
12. Yang, C. H. et al. Spin-valley lifetimes in a silicon quantum dot with tunable valley splitting. *Nat. Commun.* **4**, 2069 (2013).
13. Fock, V. Bemerkung zur Quantelung des harmonischen Oszillators im Magnetfeld. *Z. für Phys. A Hadrons Nucl.* **47**, 446–448 (1928).
14. Darwin, C. G. in *Mathematical Proceedings of the Cambridge Philosophical Society*, vol. 27, 86–90 (Cambridge University Press, 1931).
15. Zwanenburg, F. A. et al. Silicon quantum electronics. *Rev. Mod. Phys.* **85**, 961–1019 (2013).
16. Ngo, C. Y., Yoon, S. F., Fan, W. J. & Chua, S. J. Effects of size and shape on electronic states of quantum dots. *Phys. Rev. B* **74**, 245331 (2006).
17. Harting, J., Müllen, O. & Borrmann, P. Interplay between shell effects and electron correlations in quantum dots. *Phys. Rev. B* **62**, 10207 (2000).
18. Lim, W. H. et al. Spin filling of valley-orbit states in a silicon quantum dot. *Nanotechnology* **22**, 335704 (2011).
19. Borselli, M. G. et al. Measurement of valley splitting in high-symmetry Si/SiGe quantum dots. *Appl. Phys. Lett.* **98**, 123118 (2011).
20. Yang, C. H. et al. Orbital and valley state spectra of a few-electron silicon quantum dot. *Phys. Rev. B* **86**, 115319 (2012).
21. Jacak, L., Hawrylak, P., Wojs, A., Wójcik, A. & Wojs, A. *Quantum Dots* (Springer Science & Business Media, 2013).
22. Folk, J. et al. in *Quantum Chaos Y2K*, 26–33 (World Scientific, 2001).
23. Haldane, F. D. M. Continuum dynamics of the 1-d heisenberg antiferromagnet: identification with the o (3) nonlinear sigma model. *Phys. Lett. A* **93**, 464–468 (1983).
24. Brennen, G. K. & Miyake, A. Measurement-based quantum computer in the gapped ground state of a two-body hamiltonian. *Phys. Rev. Lett.* **101**, 1–4 (2008).
25. Bartlett, S. D., Brennen, G. K., Miyake, A. & Renes, J. M. Quantum computational renormalization in the haldane phase. *Phys. Rev. Lett.* **105**, 10–13 (2010).
26. Miyake, A. Quantum computation on the edge of a symmetry-protected topological order. *Phys. Rev. Lett.* **105**, 1–4 (2010).
27. Senko, C. et al. Realization of a quantum integer-spin chain with controllable interactions. *Phys. Rev. X* **5**, 1–9 (2015).
28. Higginbotham, A. P., Kuemmeth, F., Hanson, M. P., Gossard, A. C. & Marcus, C. M. Coherent operations and screening in multielectron spin qubits. *Phys. Rev. Lett.* **112**, 26801 (2014).
29. Elzerman, J. M. et al. Single-shot read-out of an individual electron spin in a quantum dot. *Nature* **430**, 431–435 (2004).
30. Koppens, F. H. L. et al. Driven coherent oscillations of a single electron spin in a quantum dot. *Nature* **442**, 766 (2006).
31. Veldhorst, M. et al. An addressable quantum dot qubit with fault-tolerant control-fidelity. *Nat. Nanotechnol.* **9**, 981–985 (2014).
32. Pla, J. J. et al. A single-atom electron spin qubit in silicon. *Nature* **489**, 541–545 (2012).
33. Pioro-Ladrière, M. et al. Electrically driven single-electron spin resonance in a slanting Zeeman field. *Nat. Phys.* **4**, 776–779 (2008).
34. Tokura, Y., Van Der Wiel, W. G., Obata, T. & Tarucha, S. Coherent single electron spin control in a slanting zeeman field. *Phys. Rev. Lett.* **96**, 047202 (2006).
35. Kawakami, E. et al. Electrical control of a long-lived spin qubit in a Si/SiGe quantum dot. *Nat. Nanotechnol.* **9**, 666–670 (2014).
36. Knill, E. et al. Randomized benchmarking of quantum gates. *Phys. Rev. A* **77**, 12307 (2008).
37. Magesan, E., Gambetta, J. M. & Emerson, J. Scalable and robust randomized benchmarking of quantum processes. *Phys. Rev. Lett.* **106**, 180504 (2011).
38. Nowack, K. C., Koppens, F. H. L., Nazarov, Y. V. & Vandersypen, L. M. K. Coherent control of a single electron spin with electric fields. *Science* **318**, 1430–3 (2007).
39. Corra, A. et al. Electrically driven electron spin resonance mediated by spin-valley-orbit coupling in a silicon quantum dot. *npj Quantum Inf.* **4**, 6 (2018).
40. Kha, A., Joyst, R. & Culcer, D. Do micromagnets expose spin qubits to charge and Johnson noise? *Appl. Phys. Lett.* **107**, 172101 (2015).
41. Zhao, R. et al. Single-spin qubits in isotopically enriched silicon at low magnetic field. *Nat. Commun.* **10**, 5500 (2019).
42. Watson, T. et al. A programmable two-qubit quantum processor in silicon. *Nature* **555**, 633 (2018).
43. Hwang, J. C. C. et al. Impact of g-factors and valleys on spin qubits in a silicon double quantum dot. *Phys. Rev. B* **96**, 045302 (2017).
44. Srinivasa, V., Nowack, K. C., Shafiee, M., Vandersypen, L. M. K. & Taylor, J. M. Simultaneous spin-charge relaxation in double quantum Dots. *Phys. Rev. Lett.* **110**, 196803 (2013).
45. Borjans, F., Zajac, D. M., Hazard, T. M. & Petta, J. R. Single-spin relaxation in a synthetic spin-orbit field. *Phys. Rev. Appl.* **11**, 044063 (2019).

46. Hao, X., Ruskov, R., Xiao, M., Tahan, C. & Jiang, H. Electron spin resonance and spin-valley physics in a silicon double quantum dot. *Nat. Commun.* **5**, 3860 (2014).
47. Amasha, S. et al. Electrical control of spin relaxation in a quantum dot. *Phys. Rev. Lett.* **100**, 046803 (2008).
48. Rashba, E. I. Theory of electric dipole spin resonance in quantum dots: mean field theory with Gaussian fluctuations and beyond. *Phys. Rev. B* **78**, 195302 (2008).
49. Takeda, K. et al. A fault-tolerant addressable spin qubit in a natural silicon quantum dot. *Sci. Adv.* **2**, e1600694 (2016).
50. Martins, F. et al. Negative spin exchange in a multielectron quantum dot. *Phys. Rev. Lett.* **119**, 227701 (2017).
51. Yang, C. et al. Silicon quantum processor unit cell operation above one kelvin. Preprint at <https://arxiv.org/abs/1902.09126> (2019).
52. Lange, K. K., Tellgren, E. I., Hoffmann, M. R. & Helgaker, T. A paramagnetic bonding mechanism for diatomics in strong magnetic fields. *Science* **337**, 327–331 (2012).

Acknowledgements

We acknowledge support from the US Army Research Office (W911NF-17-1-0198), the Australian Research Council (CE170100012), and the NSW Node of the Australian National Fabrication Facility. The views and conclusions contained in this document are those of the authors and should not be interpreted as representing the official policies, either expressed or implied, of the Army Research Office or the U.S. Government. The U.S. Government is authorized to reproduce and distribute reprints for Government purposes notwithstanding any copyright notation herein. J.C. and M.P. acknowledge support from the Canada First Research Excellence Fund and in part by the National Science Engineering Research Council of Canada. K.Y.T. acknowledges support from the Academy of Finland through project Nos. 308161, 314302 and 316551.

Author contributions

R.C.C.L. and C.H.Y. performed the experiments. J.C.L., R.C.C.L., J.C.C.H., C.H.Y. and M.P.-L. designed the micromagnet, which was then simulated by J.C.L. and M.P.-L. J.C.C.H. and F.E.H. fabricated the device with A.S.D.’s supervision. K.W.C. and K.Y.T. contributed to discussion on nanofabrication process. K.M.I. prepared and supplied the ²⁸Si epilayer. J.C.C.H., W.H. and T.T. contributed to the preparation of experiments.

R.C.C.L., C.H.Y., A.S. and A.S.D. designed the experiments, with J.C.L., M.P.-L., W.H., T.T., A.M. and A.L. contributing to results discussion and interpretation. R.C.C.L., A.S. and A.S.D. wrote the paper with input from all co-authors.

Competing interests

The authors declare the following competing interests: This work was funded, in part, by Silicon Quantum Computing Proprietary Limited.

Additional information

Supplementary information is available for this paper at <https://doi.org/10.1038/s41467-019-14053-w>.

Correspondence and requests for materials should be addressed to R.C.C.L., A.S. or A.S.D.

Peer review information *Nature Communications* thanks the anonymous reviewers for their contribution to the peer review of this work.

Reprints and permission information is available at <http://www.nature.com/reprints>

Publisher’s note Springer Nature remains neutral with regard to jurisdictional claims in published maps and institutional affiliations.



Open Access This article is licensed under a Creative Commons Attribution 4.0 International License, which permits use, sharing, adaptation, distribution and reproduction in any medium or format, as long as you give appropriate credit to the original author(s) and the source, provide a link to the Creative Commons license, and indicate if changes were made. The images or other third party material in this article are included in the article’s Creative Commons license, unless indicated otherwise in a credit line to the material. If material is not included in the article’s Creative Commons license and your intended use is not permitted by statutory regulation or exceeds the permitted use, you will need to obtain permission directly from the copyright holder. To view a copy of this license, visit <http://creativecommons.org/licenses/by/4.0/>.

© The Author(s) 2020